Microsyst Technol (2011) 17:1025–1036
DOI 10.1007/s00542-011-1276-0

TECHNICAL PAPER

A new energy harvest system with a hula-hoop transformer, micro-generator and interface energy-harvesting circuit

Paul C.-P. Chao · C. I. Shao · C. X. Lu · C. K. Sung

Received: 31 August 2010 / Accepted: 9 March 2011 / Published online: 29 March 2011

Abstract This study presents a synthesis of a new energy harvest system that consists of a hula-hoop transformer, a micro-generator and an interface energy harvest circuit. The hula-hoop transformer mainly comprises a main mass sprung in one translational direction and a free-moving mass attached at one end of a rod, the other end of which is hinged onto the main mass. The transformer is capable of transforming linear reciprocating motions to rotary ones based on the concepts similar to the hula hoop motions. The transformer is subsequently integrated with a miniaturized rotary generator in size of $10 \times 10 \times 2$ mm^3 and its compact energy harvest circuit chip. The designed generator consists of patterned planar copper coils and a multi-polar hard magnet ring made of NdFeB. The genetic algorithm (GA) is next applied to optimize the critical dimensions of the miniaturized generator. The optimized generator offers 4.5 volt and 7.23 mW in rms at 10,000 rpm. With micro-generator successfully fabricated, a novel energy harvest circuit employing a new dual phase charge pump, power management circuit, a low dropout regulator and battery charger is designed and fabricated via the 0.35 μm process. This charge pump circuit owns the merit of automatic conversion of low-power AC signals by the micro-generator to DC ones. Experiments were conducted to show the favorable performance of the proposed energy harvest system. This is the first work that invents a motion transformer from ubiquitous reciprocating to rotational motions. In this way, higher-efficient energy conversion via compact-sized rotational electromagnetic generators can be realized as opposed to popular piezoelectric structures.

P. C.-P. Chao (✉) · C. I. Shao
Department of Electrical Engineering,
National Chiao Tung University, Hsinchu 300, Taiwan
e-mail: pchao@mail.nctu.edu.tw

P. C.-P. Chao
Institute of Imaging and Biomedical Photonics,
National Chiao Tung University, Tainan 711, Taiwan

C. X. Lu · C. K. Sung
Department of Power Mechanical Engineering,
National Tsing Hua University, Hsinchu 300, Taiwan

1 Introduction

Energy harvesting methods such as RF powered systems (Sudou et al. 2008), solar powered systems, motional energy harvesting systems (Jose et al. 2001), thermoelectric powered systems (Leonov et al. 2007), and piezoelectric conversion systems (Ottman et al. 2003) can be used to collect energy from a controlled or ambient environment, to power devices directly or store the energy in battery cells for later use. The benefits of the application systems with an energy harvest unit are that recharging battery is not necessary while the devices or modules are expected to be operated for an extended time.

One of the most effective methods of implementing an energy harvesting system is the use of mechanical vibration. For example, the electromagnetic vibro-generators produce electricity with moving permanent magnets as the armature and fixed coils as the stator (Kulah and Najafi 2008). Arnold (2007) proposed three types of electromagnetic power generation systems in the range of microwatts to tens of watts. Sasaki et al. (2005) proposed a device that is combined with gear train to generate power under the state of self-excited rotation. Spreemann et al. (2006) also presented an electricity-generating device with the volume 1.5 cm^3 and power 0.4–3 mW at vibration frequencies of 30–80 Hz. The above devices generated electricity based

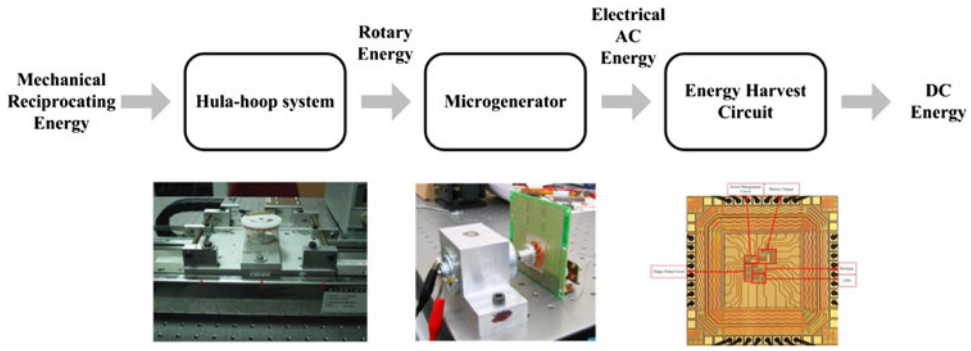

Fig. 1 The synthesized energy harvest system

on vertical oscillation that takes gravity into consideration. Yoshitake et al. (2004) proposed a device on the basis of hula-hoop motion for the purpose of quenching machine vibration while harvesting electricity. Hatwal et al. (1983) focused on the dynamic analysis of similar model considering a small-amplitude oscillation of the free mass which is different from this work. Shaw et al. (2006) presented an analytical investigation of centrifugal pendulum vibration absorber called tautochronic vibration absorbers for reducing torsional vibrations in rotating systems following the specified paths.

This study presents the synthesis of a new energy harvest system, as show in Fig. 1. It consists of a hula-hoop transformer, micro-generator and an interface energy-collecting circuit. The proposed system is capable of collecting ubiquitous environmental reciprocating energy into eventually a DC battery. This is made possible by (1) a hula-hoop transformer (Lu et al. 2009) that converts translational vibrations to rotaries; (2) a miniaturized micro-generator (Liao et al. 2009) with coils to transfer the aforementioned mechanical vibrations to electrical current; (3) finally, an interface analog circuit is designed and fabricated to charge a Li-Ion battery for storing the harvested energy. Experiments were conducted to show the favorable performance of the proposed energy harvest system. Note that this is the first work that invents a motion transformer from reciprocating to rotational motions. In this way, higher-efficient energy conversion via compact-sized rotational electromagnetic generators can be realized as opposed to popular piezoelectric structures.

2 Hula-hoop transformer

2.1 Dynamic modeling and approximate solutions

Mimicking the hula-hoop motion, this study proposes a novel motion transformer design, as shown in Fig. 2 (Lu et al. 2009), which consists of a main mass sprung in the y-direction and a free-moving mass attached at one end of a rod, the other end of which is hinged onto the center of the main mass.

In Fig. 2, M, m, k, c, c_m, R_m and F denote the main mass, free mass, coefficient of the spring, damping capacity of the damper, rotational damping due to the friction between the pin and hole, rotational radius between the center of the free mass and the pin, and the excitation force applied in the y-direction, respectively. The main mass is confined to move only in the y-direction. The free mass is assumed to be a semicircle thin plate in Fig. 2. The main and free masses move parallel to the ground; no gravitational force acts on them. The equations governing the motion of the main mass and free mass are written as

$$(M+m)\ddot{y} + mR_m(\ddot{\theta}\cos\theta - \dot{\theta}^2\sin\theta) + c\dot{y} + ky = F\cos(\omega t), \quad (1)$$

and

$$(mR_m^2 + I)\ddot{\theta} + c_m\dot{\theta} = -mR_m\ddot{y}\cos\theta, , \quad (2)$$

where I is the mass moment of inertia of the semi-circular thin plate, y denotes the reciprocating motion of the main mass and θ the rotational angle of the free mass. Equations (1) and (2) are expressed in non-dimensional forms for conveniently analyzing the dynamic behaviors of the system,

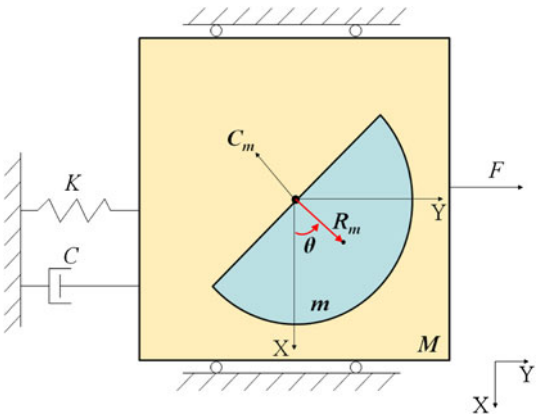

Fig. 2 Physical model of hula-hoop motion with a semi-circular thin plate as the free masses

$$q''(\tau) + 2\rho q'(\tau) + q(\tau) + \varepsilon[\theta''(\tau)\cos\theta(\tau) - (\theta'(\tau))^2 \sin\theta(\tau)] = F_{eq}(\tau), \quad (3)$$

and

$$(1 + I_{eq})\theta''(\tau) + \xi_m\theta' + q''(\tau)\cos\theta(\tau) = 0, \quad (4)$$

where

$$\tau = \omega_n t,\ \omega_n = \sqrt{\frac{k}{M+m}}, q(\tau) = y(t)/R_m,$$
$$q'(\tau) = \dot{y}(t)/R_m\omega_n, \theta(\tau) = \theta(t), \theta'(\tau) = \dot{\theta}(t)/\omega_n,$$
$$\varepsilon = \frac{m}{M+m}, F_{eq}(\tau) = \frac{F\cos(\alpha\tau)}{(M+m)R_m\omega_n^2}, \alpha = \omega/\omega_n,$$
$$\rho = \frac{c}{2(M+m)\omega_n}, \varsigma_m = \frac{c_m}{mR_m^2\omega_n}, I_{eq} = \frac{9\pi^2}{32} - 1$$

Note also in the aboves that the prime denotes the derivative with respect to the non-dimensional time τ. ω_n and ω are the natural frequency of the system and the excitation frequency, respectively. In addition, α is the non-dimensional frequency of excitation, and ε the mass ratio of the system. ρ and ς_m denote the dimensionless system damping and rotational damping, respectively. Additionally, I_{eq} is the mass inertia of the free mass. Accordingly, the approximate steady-state solutions of main mass and free mass are presented as

$$V_q(\tau) = V_{0q} + V_{1q} = q_1\cos(\alpha\tau - \beta), \quad (5)$$

and

$$V_\theta(\tau) = V_{0\theta} + V_{1\theta} = \alpha\tau + u_1\cos(2\alpha\tau - \gamma), \quad (6)$$

with four unknowns q_1, u_1, β, γ as shown below,

$$q_1 = Tu_1, \quad (7)$$

$$u_1 = \frac{\varepsilon\alpha^2}{(1-\alpha^2)T\sin\beta - 2\rho\alpha T\cos\beta}, \quad (8)$$

$$\beta = \tan^{-1}\left\{\frac{\varepsilon\alpha^2\left[(1-\alpha^2)T - \frac{1}{2}\varepsilon\alpha^2\cos\phi\right] + 2F_{eq}\rho\alpha T}{\varepsilon\alpha^2\left[-2\rho\alpha T + \frac{1}{2}\varepsilon\alpha^2\sin\phi\right] + F_{eq}(1-\alpha^2)T}\right\}, \quad (9)$$

$$\gamma = \beta - \phi, \quad (10)$$

where

$$T = -4\sqrt{4(1+I_{eq})^2 + \frac{\varsigma_m^2}{\alpha^2}} \quad (11)$$

$$\phi = \tan^{-1}\left(\frac{\varsigma_m}{2\alpha(1+I_{eq})}\right). \quad (12)$$

2.2 Stability and operation principles

The result of investigating stability of approximate solutions is presented in Fig. 3a with different combinations of excitation amplitudes and frequencies. The zone II with blue o's is stable. Within the blue region, the hula-hoop motion happens. The main mass reciprocates with frequency ω. The free mass revolves with frequency ω and the oscillation frequency 2ω. Furthermore, the stability of the system in relation with the amplitude of initial approximate solution of free mass u_1 are also discussed. The zones I with red ×'s, yellow ×'s, and black ×'s are unstable. The hula-hoop motion does not exist. In the unstable regions, red, yellow, and black ×'s feature $|u_1| < 0.5, 0.5 < |u_1| < 1$, and $|u_1| > 1$, respectively. Although, the red zone featured $|u_1| < 0.5$, it accompanies with reversal motions for the system. However, through increasing the value of $|u_1|$, the system possesses larger reversal motions. Thus, it is necessary to keep $|u_1| < 0.5$ to assure of the existence of hula-hoop motion.

Figure 3b illustrates the solutions of hula-hoop motion obtained from direct numerical integration with Eqs. (1) and (2). Good agreement between Figs. 3a and b proves the effectiveness of solutions methods. In Fig. 3b, the regions with blue o's are accompanied with the hula-hoop motions. However, the zones I and III with red ×'s have no hula-hoop motions. Moreover, the transition regions featured cyan +'s show the reversal motions existed in this area, and the areas with cyan o's present the hula-hoop motion is attained at the transient state but does not exist at the final steady state. Furthermore, blue +'s also show the reversal motions but with similar oscillating frequency to 2α. From the result, it can also be observed that the reversal motion is happened more easily with larger excitation.

In addition, there exists the region III featured red ×'s which is not showed in Fig. 3a. In the derivation of approximate solutions, the harmonic terms with lowest oscillating frequency 2α are only considered without including the effect of higher-order harmonic terms. Furthermore, the free mass possesses circular motions instead of oscillatory motions performed by simple pendulums in this study, so the nonlinear term $q''\cos\theta$ of Eq. (4) cannot be linearized (Belendez et al. 2007). Thus, the zone for low excitation amplitude where the hula-hoop motion is not present may be less accurate than oscillatory motions of simple pendulum. Additionally, the eigenvalues at the region of low excitation amplitude are close to unity; herein, the hula-hoop motion could not be defined as steady-state motion because it may changes to another motion as it was perturbed. Additionally, the comparison of numerical results and experimental results will be discussed in the Experimental session.

3 Miniaturized micro-generator

3.1 System design and fabrication

The micro-generator is designed and fabricated for combining the hula-hoop transformer as a self-power system to

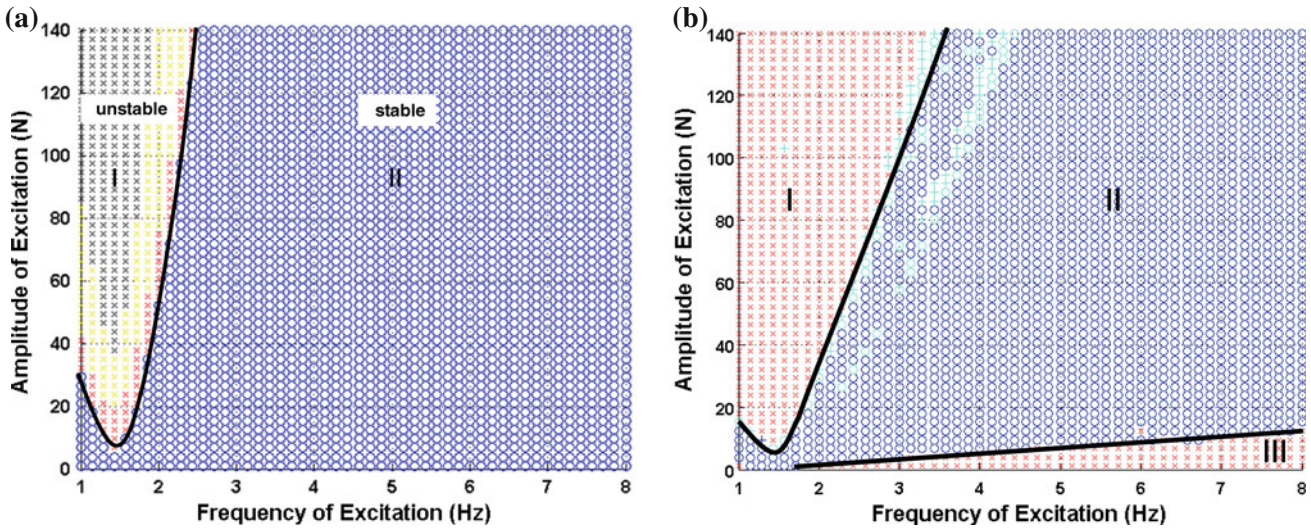

	Blue (○)	Red (×)	Yellow (×)	Black (×)
$\lvert u_i \rvert$	$\lvert u_i \rvert$<0.5	$\lvert u_i \rvert$<0.5	0.5<$\lvert u_i \rvert$<1	$\lvert u_i \rvert$>1
Hula-hoop motion	Yes	No	No	No

	Blue (o)	Blue (+)	Cyan (o)	Cyan (+)	Red (×)
Hula-hoop motion	Yes	No	No	No	No
Reversal	No	Yes	No	Yes	
Freq. α	≒ 1ω	≒ 1ω	≒ 1ω	≒ 1ω	
Freq. *fu*	≒ 2ω	≒ 2ω	≠2ω	≠2ω	

Fig. 3 **a** Stability of the approximate solutions. **b** Occurrence of Hula-hoop motion obtained from direct numerical simulation

scavenge energy from rotational vibrations. It consists of patterned planar copper coils and a multi-polar hard magnet ring. The schematic illustration of the entire micro-generator is shown in Fig. 4. In this figure, eight coils correspond to eight S and N poles, which are realized by a magnetized segments of NdFeB embedded in a rotating rotor ring. The pattern of each coil is designed as sector-shape loops. The copper coil is fixed as a stator, which is protected by the plastic films, while the magnet is rotatable as a rotor, which is shaped as a ring. It is noted that the thickness of plastic film is very thin compared to the thickness of copper coil denoted by *t*. Thus, it can be neglected in simulation process. The eight-pole magnets is fabricated by using the sintering technology, and the NdFeB magnet is magnetized by using the custom-designed stator. A satisfactory performance of a hard magnet is rendered with a residual induction (Br) of 1.1 T and a coercive force (Hc) of 910 k Am. In order to obtain a fast prototype, the method of filament winding is adopted to fabricate the coils which is impregnated on the 50 μm polyethylene terephthalate (PET) substrate. Eight planar coils with a single filament of copper wire are successfully manufactured in this study. The resistivity of the copper planar miniaturized coils is 1.7 Ω/10 m.

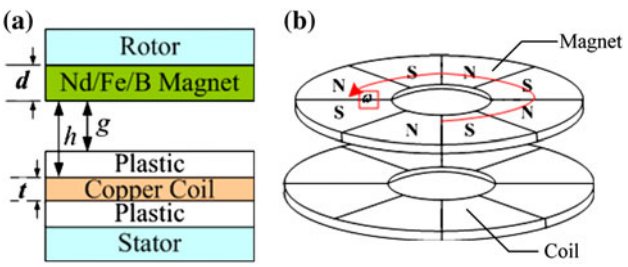

Fig. 4 **a** Internal structure and materials of the generator. **b** A 3-D schematic of the generator

3.2 Theoretical analysis

In order to predict the induced voltage and the resulted power produced by the micro-generator, the theoretical modeling with the assistance of finite-element simulation via software ANSYS is performed in this section.

In the beginning, one single coil sector is considered as shown in Fig. 5a. In this figure, four vertices are denoted as a, b, c and d. The distance between the internal edge of the coil sector and the stator center, the radial coil sector span, and the coil width are denoted as *r*, *b* and *w*, respectively. It is noted that when the rotor is rotating, the induced magnetic flux cross the segments of a–b and c–d will induce

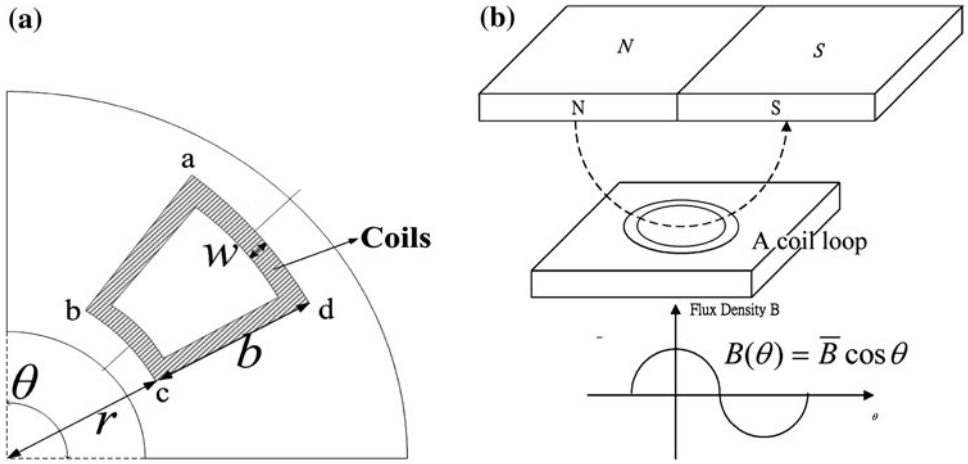

Fig. 5 **a** Dimensions of one single sectoral coil loop in the stator. **b** Illustration of magnetic flux and its density change along θ

electromotive force (EMF) voltages. However, the directions of segments d–a and b–c are parallel to the flux, which will not produce any voltage. According to Fleming's right-hand side rule, the induced current will flow from d to c and b to a. Therefore, the next is to compute the EMF voltage induced by the crossing of magnetic flux over the coils

Considering a pair of N and S magnetic poles and one coil sector as shown in Fig. 5b, the induced EMF voltage V_{emf} is equal to the change rate of total magnetic flux ϕ as the magnet poles are moving horizontally, which is based on the well-known Faraday's law. Therefore, the induced EMF voltage can be derived as

$$V_{emf}(t) - \frac{d}{dt}\int_s B(\theta)\cdot dA = -\int_s \frac{\partial B(\theta)}{\partial t}\cdot dA, \tag{13}$$

where $B(\theta)$ is the magnetic flux density along the circumferential direction of the rotor ring and coils, and A is the area enclosed by a single coil loop. Assuming each coil loop owns the same shape and size. Thus, Eq. (13) becomes

$$V_{emf}(t) = -\frac{d\phi(t)}{dt} = 4n\omega\overline{B}A\sin\omega t, \tag{14}$$

where $\overline{B}$ is the magnitude of the flux density variation over one single coil loop, n is the number of terns for a single coil sector, and ω is the rotor's rotational speed. With measured $\overline{B}$, the induced EMF voltage can be estimated by the above equation, and the magnitude of the induces EMF is thus $4n\omega\overline{B}A$.

The output power is the ratio of root mean square (rms) of the induced EMF voltage V_{emf} over the net coil resistance of the generator R_{coil}; thus,

$$P = \frac{V_{rms}^2}{2R_{coil}}, \tag{15}$$

where V_{rms} can be calculated by the previous derived (14). The net coil resistance R_{coil} is computed based on the proportionality to the total length of the coils, which is in fact

$$R_{coil} = \frac{\rho L}{\hat{A}} = \frac{\rho L}{\hat{A}}(4\pi r + 16b), \tag{16}$$

where L is the coil length, $\hat{A}$ is the cross section of the coil, ρ is the copper resistance per unit volume, r is the distance between the internal edge of the coil sector and the stator, and b is the radial coil sector span.

3.3 Experimental validation

The micro-generator is fabricated for experimental validation in this section. The photographs of the fabricated micro-generator are shown in Fig. 6a and b. Meanwhile,

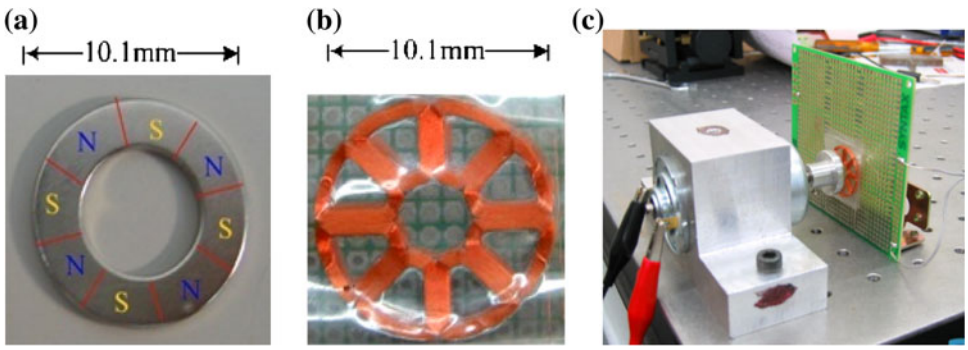

Fig. 6 **a** The magnet ring as a rotor. **b** The fabricated planar coil as a stator. **c** Measurement set-up

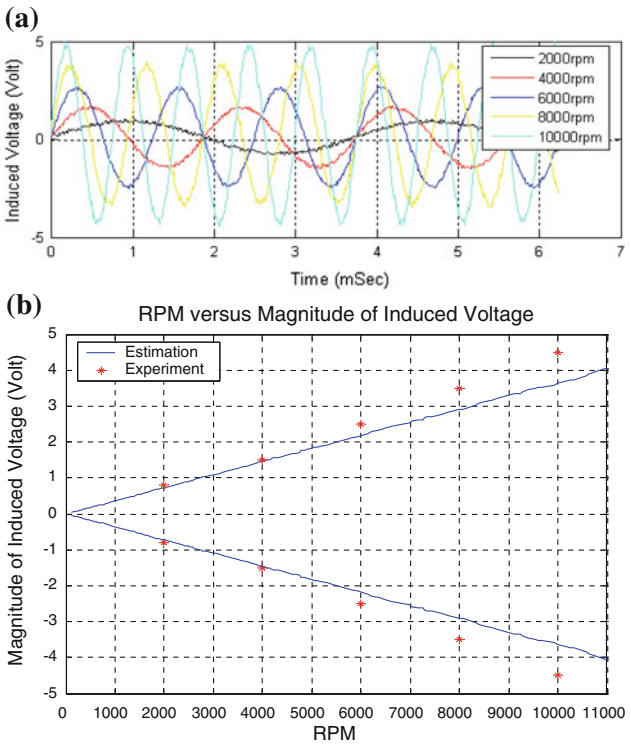

Fig. 7 **a** Experimental induced voltage. **b** Induced voltage amplitude

the measurement set-up of the micro-generator is shown in Fig. 6c. In this figure, the magnet and the coil is fixed on a rotary mechanism and attached on a static platform, respectively. The gap between each other is set to 1 mm. The rotary mechanism is driven by the power supply to make the multi-polar magnet rotate at different angular velocity or frequency. When the eight-polar magnet is rotated relative to Cu micro-coil, the planar micro-coil induces voltage and current. Figure 7a shows the measured induced voltage with different rotational speeds. The resistive load is 1.4 kΩ for matching the coil resistance. It can be seen from this figure that the magnitudes of the induced voltage is increased with higher rotational speed. Besides, the magnitudes of the induced voltages are presented in Fig. 7b. It is noted that the magnitude of the induced voltage is almost linear compared to the rotor speed, which is confirmed by Eq. (14). Measurement shows that the micro-generator induces a realistic peak voltage of 4.5 V and offers a maximum power output of 7.23 mW at 10,000 rpm.

4 Energy harvest circuit

A new energy harvest circuit is developed in this study to harvest the electrical power generated by the micro-generator. This circuit consists of (1) the proposed novel charge pump circuit (Fig. 8), (2) power management circuit (Fig. 9), (3) low drop out (LDO) circuit (Fig. 10) and (4) battery charger circuit (Fig. 11). The new designed charge pump circuit not only rectifies the input AC signal power but also boosts up the voltage in a single-cycle fashion which is supposed to be much faster than a traditional Dickson charge pump circuit (Dickson 1976) employing a cyclic charging operation. The clock generator used in

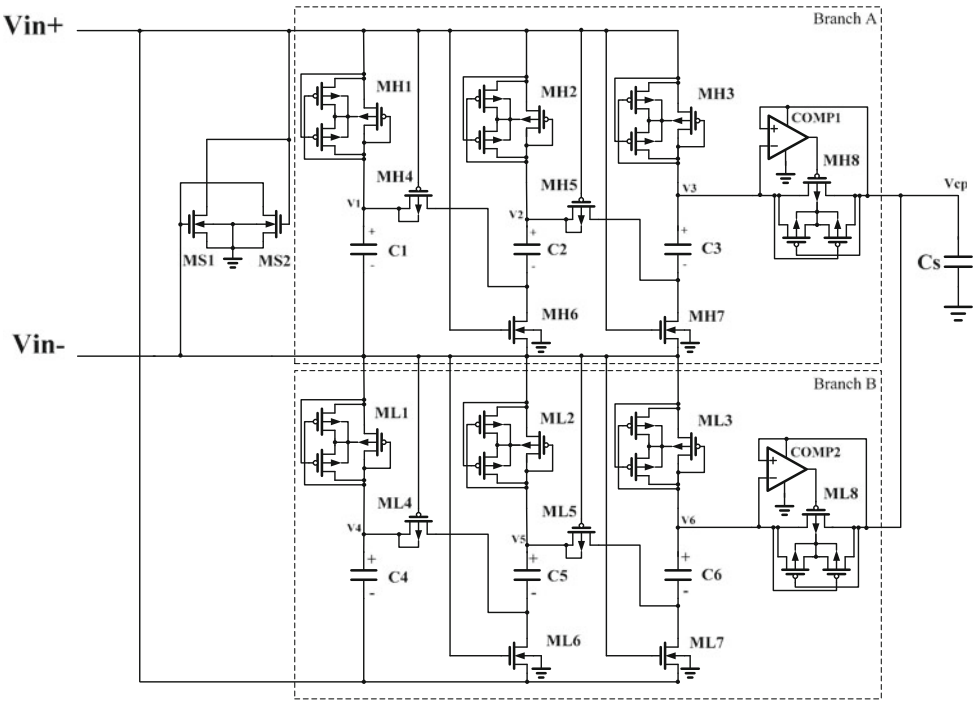

Fig. 8 Dual phase charge pump circuit

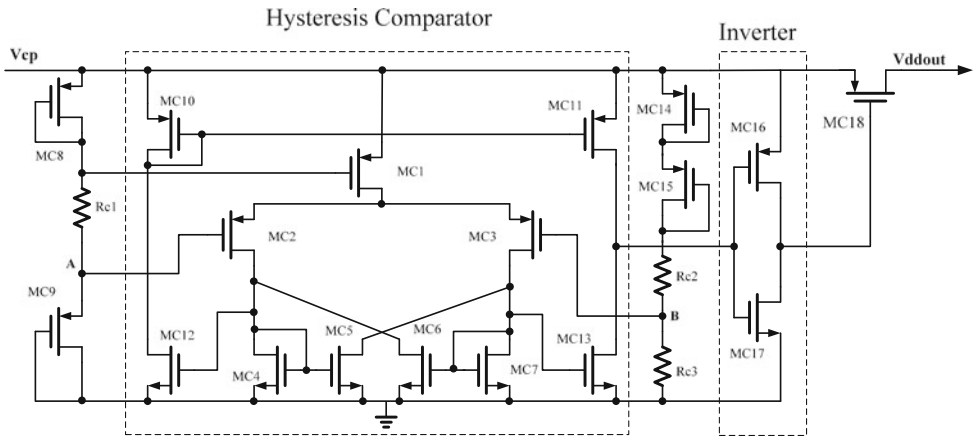

Fig. 9 Power management circuit

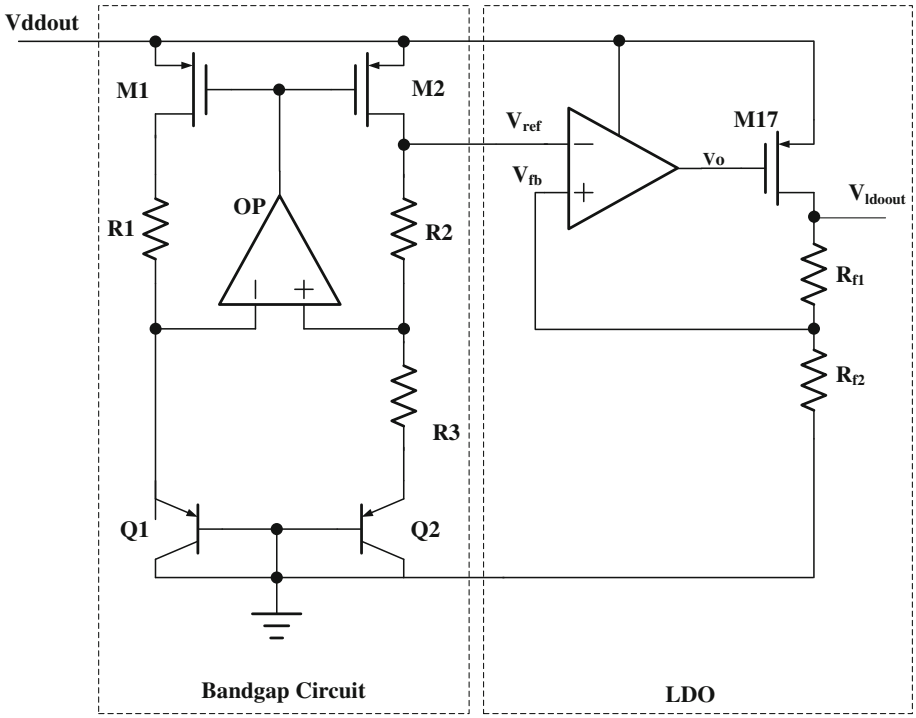

Fig. 10 Low dropout (LDO) circuit

traditional charge pump circuits is not a necessity in the proposed novel charge pump circuit. In other words, no external control signal is needed, which is suitable for the design of the low power energy harvest circuit without the assistance of external power source. The power management circuit monitors the amount stored energy and decide whether the energy stored in the capacitor is sufficient to supply for output or not. The LDO regulates the varying output voltage of the power management circuit to a steady DC voltage and reducing the load effect. Finally, a fast battery charger is designed to transform the energy generated by the hula-hoop transformer and micro-generator into Li-Ion battery.

4.1 Dual phase charge pump

Since the output voltage of the micro-generator is not sufficiently high to drive the battery charger circuit, it is necessary to boost up the voltage. Thus, a three-stages novel charge pump circuit is proposed in this study, as shown in Fig. 8. There are two identical branches, labeled as branches A and B. These two branches are combined in order to fulfill the dual phase output, which can reduce the output ripple and increase the output driving capability. The basic concept of the charge pump circuit is that all capacitors of branch A or branch B are charged in parallel and discharged in series within one single cycle, respectively.

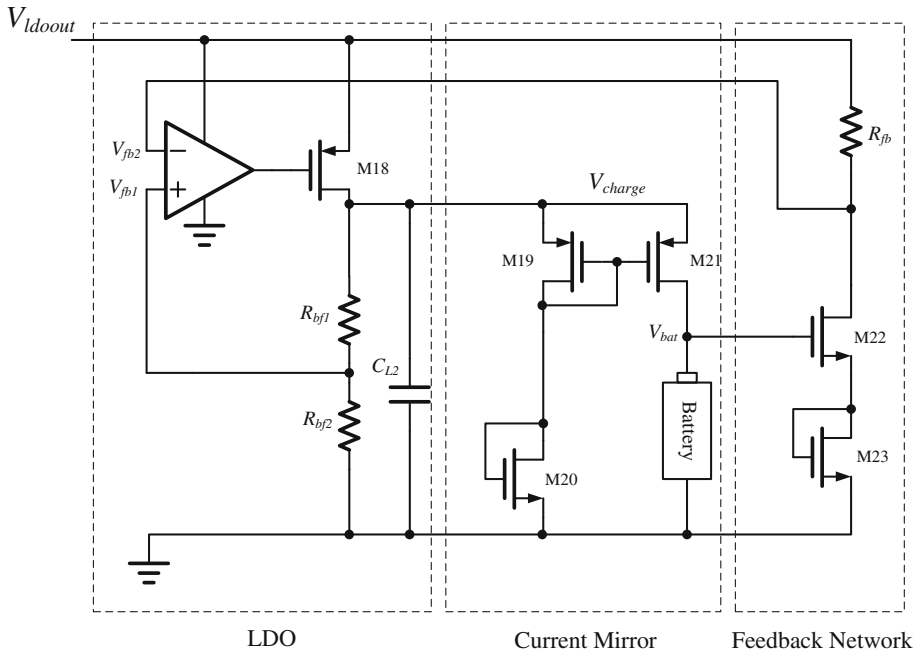

Fig. 11 Battery charger circuit

4.1.1 Operation principles

4.1.1.1 For the state 1 of positive input signal Assuming that all capacitors have zero voltage in the initial condition. When the input signal exceeds the NMOS threshold voltage, MH6 and MH7 turn on. MS2 also turns on, so that V_{in-} is connected to ground. While MH4 and MH5 turn off. When the forward voltage (V_{DS}) exceeds the PMOS threshold voltage. Diode-connected PMOS MH1, MH2 and MH3 start to conduct current. At this moment, all capacitors of branch A are connected in parallel. Therefore, C1, C2 and C3 are charged to ($V_p - V_{THP}$).

On the other hand, MS1, ML6 and ML7 turn off as the input signal is smaller than the NMOS threshold voltage. While ML4 and ML5 turn on and the diode-connected PMOS ML1, ML2 and ML3 block in the condition of

$$V_4 - V_{in-} > |V_{THP}| \tag{17}$$

and

$$V_5 - V_{in-} > |V_{THP}|, \tag{18}$$

where V_{THP} is the PMOS threshold voltage. At this moment, all capacitors of branch B are connected in series. Therefore, C4, C5 and C6 boost up the input voltage and deliver charges from V_{in+} to V_6. As a result, the output voltage can be derived as

$$V_6 = V_{in+} + V_{C4} + V_{C5} + V_{C6}, \tag{19}$$

where V_{C4}, V_{C5}, and V_{C6} are the voltage across C4, C5 and C6, respectively. Moreover, the maximum output voltage of branch B can be derived as

$$V_{6,\max} = V_p + (V_p - |V_{THP}|) + (V_p - |V_{THP}|) + (V_p - |V_{THP}|) = 3(V_p - |V_{THP}|) + V_p. \tag{20}$$

if C4, C5 and C6 were charged to ($V_p - |V_{THP}|$) in the previous state.

4.1.1.2 For the state 2 of negative input signal In state 2, MS2, MH6 and MH7 turn off as the differential input signal ($V_{in+} - V_{in-}$) is negative. While MH4 and MH5 turn on and the diode-connected PMOS, MH1, MH2 and MH3 are blocked in the condition of

$$V_1 - V_{in+} > |V_{THP}| \tag{21}$$

and

$$V_2 - V_{in+} > |V_{THP}|. \tag{22}$$

At this moment, all capacitors of branch A are connected in series. Therefore, C1, C2 and C3 boost up the input voltage and deliver charges from V_{in+} to V_3. The output voltage can be derived as

$$V_3 = V_{in-} + V_{C1} + V_{C2} + V_{C3}, \tag{23}$$

where V_{C1}, V_{C2} and V_{C3} are the voltages across C1, C2 and C3, respectively. Similarly, the maximum output voltage of branch A can be derived as

$$V_{3,\max} = V_p + (V_p - |V_{THP}|) + (V_p - |V_{THP}|) + (V_p - |V_{THP}|) = 3(V_p - |V_{THP}|) + V_p. \tag{24}$$

On the other hand, when the differential input signal ($V_{in-} - V_{in+}$) exceeds the NMOS threshold voltage, ML6 and ML7 turn on. MS1 also turns on, so that V_{in+} is

connected to ground. While ML4 and ML5 turn off. The diode-connected PMOS, ML1, ML2 and ML3, start to conduct current when the forward voltage V_{DS} exceeds the PMOS threshold voltage. At this moment, all capacitors of branch B are connected in parallel. Therefore, the capacitors C4, C5 and C6 are charged. The maximum voltage of capacitors also reach to the same voltage, $V_p - |V_{THP}|$, the same as that as the capacitors in branch A are charged in parallel in state 1.

In order to deal with the body effects, the buck regulation technology is applied in the proposed charge pump circuit (Shin et al. 2000). Furthermore, the active diode technology with comparators is utilized on the PMOS MH8 and ML8 to reduce the voltage drop across the two terminals of MOS transistors, i.e. drain node and source node (Peters et al. 2008). In conclusion, branch A and B operate in the opposite way depending on the differential input signal is positive or negative. MS1 and MS2 are used to connect V_{in+} to ground in state 2 and V_{in-} to ground in state 1, respectively. This design can make the charge pump circuit charge in parallel and discharge in series exactly and has the function of rectification.

Note that maximum power transfer from the micro-generator to the output of the designed charge pump can only be achieved if the source impedance from the micro-generator matches the input impedance of the energy harvest circuit (Shameli et al. 2007). One can tune parameter of the parasitic R and C of the designed charge rump circuit to achieve maximum power transfer. However, the tuned R and C can only be implemented by an off-line fashion.

4.2 Power management circuit

Since the power generated by the micro-generator is low, it is not sufficient to power the battery charger all the time. Therefore, the power management circuit is introduced to monitor the energy and power the battery charger periodically. The circuit diagram of the power management circuit is shown in Fig. 9. This circuit is composed of a two-stage hysteresis comparator, an inverter and a switching MOSFET, as shown in Fig. 9. It has two operation modes—standby and enable mode. In standby mode, the power management circuit stops delivering the energy form V_{cp} to V_{ddout} while the storage capacitor is charged by the charge pump circuit. When the voltage across Cs exceeds 2.8 V, the power management circuit changes to enable mode, drawing current from the storage capacitor and discharging it. The power management circuit is set back to standby mode until the voltage of the storage capacitor drops below 2.2 V.

The voltages of the anode A and the cathode B are generated by using the voltage-feedback control. MC8, MC9 and Rc1 generate a nearly constant voltage ($|V_{THP}|$) at anode A, while MC14, MC15, Rc2 and Rc3 generate a changeable voltage at cathode B depending on the voltage of the storage capacitor. The voltage of the cathode B can be derived as

$$V_B = (V_{cp} - 2|V_{THP}|) \times \frac{R_{c3}}{R_{c2} + R_{c3}}, \tag{25}$$

where V_{THP} is the PMOS threshold voltage.

4.3 Battery charger

In order to store the energy transferred by the micro-generator, a battery charger is necessarily designed for charging batteries. Therefore, a 1.2 V battery charger circuit is proposed by using the constant-current (CC) constant-voltage (CV) charge strategy to avoid undercharging or overcharging, as shown in Fig. 11. This circuit is composed of a LDO, a current mirror and a feedback network.

The basic concept of the battery charger is based on the voltage feedback rule. In the initial condition, M22 and M23 turn off when the voltage of the battery is below the rated voltage, i.e.

$$V_{bat} < 2V_{THN}, \tag{26}$$

where V_{THN} is the NMOS threshold voltage. Thus, $V_{fb2} = V_{ldoout}$. LDO outputs a high voltage nearly the supply voltage. The input current of the battery is mirrored by the current mirror circuit, which has the characteristic of constant current. The battery charger operates in the CC mode in the condition of

$$V_{fb2} > V_{fb1} = V_{charge} \times \frac{R_{bf2}}{R_{bf1} + R_{bf2}}. \tag{27}$$

When the battery voltage is equal to the rated battery voltage, M22 and M23 turn on. Thus, the feedback voltage can be derived as

$$V_{fb2} = V_{ldoout} - I_{fb} \times R_{fb}, \tag{28}$$

where I_{fb} is the current through resistor R_{fb}. At this moment, the output voltage of LDO down to the battery rated voltage in the condition of

$$V_{charge} \times \frac{R_{bf2}}{R_{bf1} + R_{bf2}} = V_{fb1} > V_{fb2}. \tag{29}$$

Therefore, the battery charger operates in the CV mode. The input current of the battery is very small, so that the battery can be fully charged to 1.2 V without the risk of overcharging.

4.4 Experimental validation

The proposed energy harvest circuit is fabricated via the TSMC 0.35 μm Mixed-Signal 2P4M process offered by

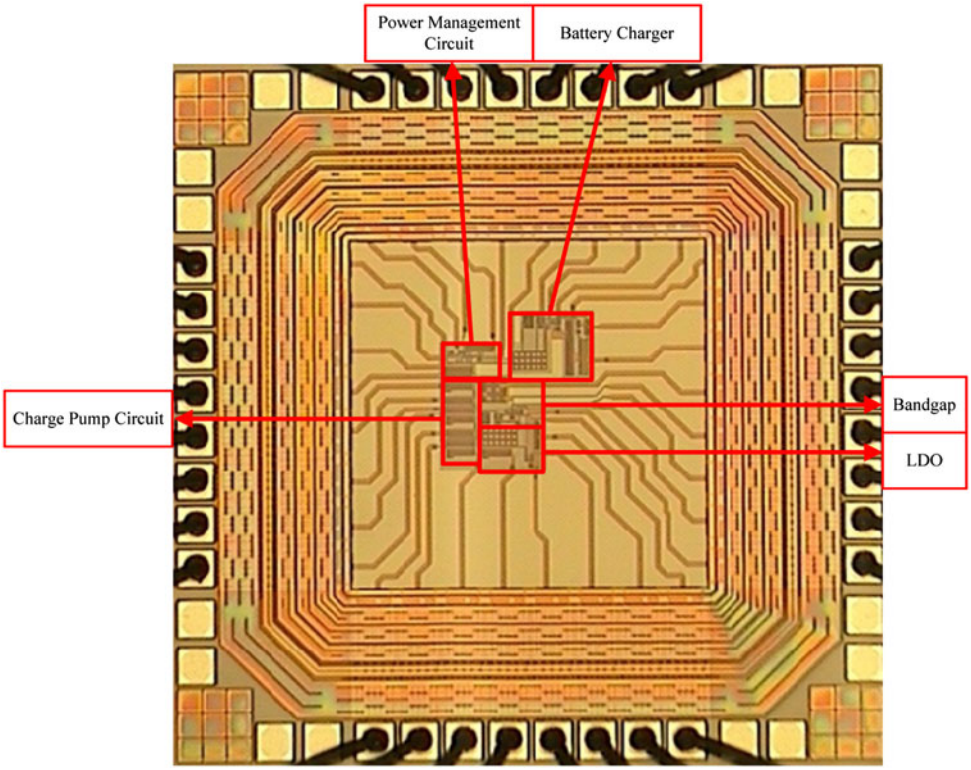

Fig. 12 Microphotograph of the energy harvest circuit

National Chip Implementation Center (CIC) of Taiwan. The microphotograph of the test chip and the measurement set-up are shown in Figs. 12 and 13, respectively. The core area of the test chip without capacitors is 0.32 mm × 0.32 mm. The responses of the dual phase charge pump circuit are shown in Fig. 14. It can see from this figure that charging and pumping are accomplished in a single-cycle fashion. On the other hand, the test results of combining the power management circuit and LDO are shown in Fig. 15. In this figure, when the voltage of the storage capacitor exceeds 2.8 V, the LDO outputs stable 1.8 V until the voltage of the storage capacitor drops below 2.2 V. Because the power management circuit is supplied by the storage capacitor directly, it is designed with very low power consumption which dissipates 2.2 μW at 2.8 V supply voltage.

Finally, the measurement results of the battery charger are shown in Fig. 16. At the front end of the entire system, the hula-hoop is operated to oscillate in 100 Hz with a main mass of 63 g. The power is then transferred through the charge pump to LDO for battery charging. For LDO, in order to emulate the internal resistance of the 1.2 V battery, one resistor R_{CELL} of 100 m is used to stand for the internal resistance. Furthermore, one capacitor C_{CELL} of 1,000 μF is used to emulate the capacity of the 1.2 V battery in order to monitor the charging process within a short period. At the beginning, the charger detects the initial voltage of the battery.

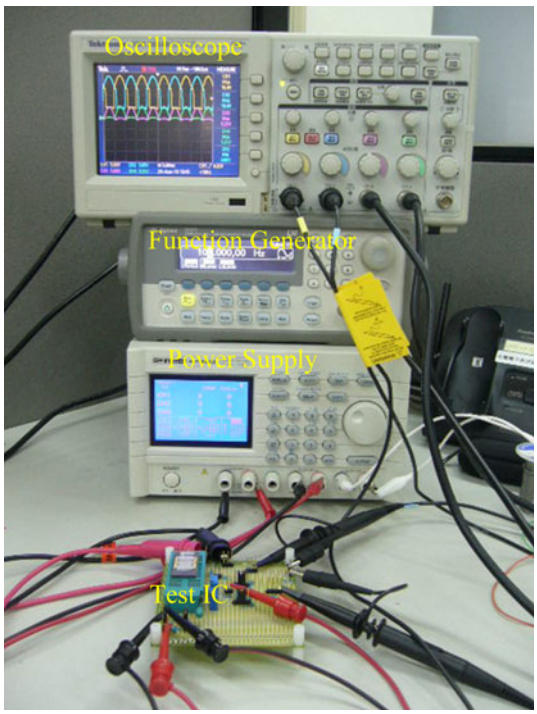

Fig. 13 Photograph of measurement set-up

Therefore, the battery is charged by the CC because of low battery voltage. It means much energy is rapidly stored in battery during CC mode. When the battery

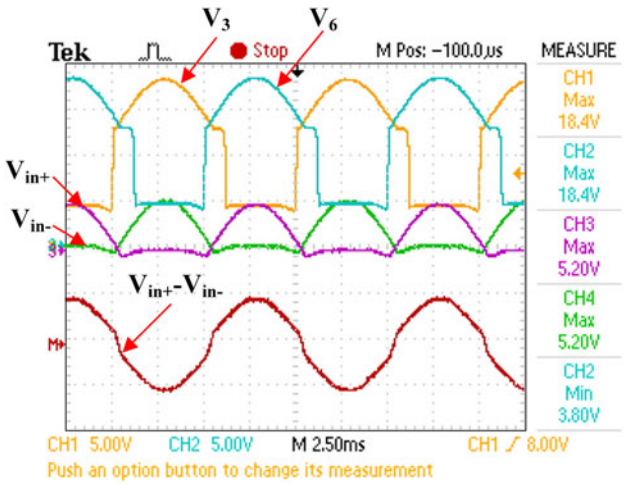

Fig. 14 Responses of dual phase charge pump

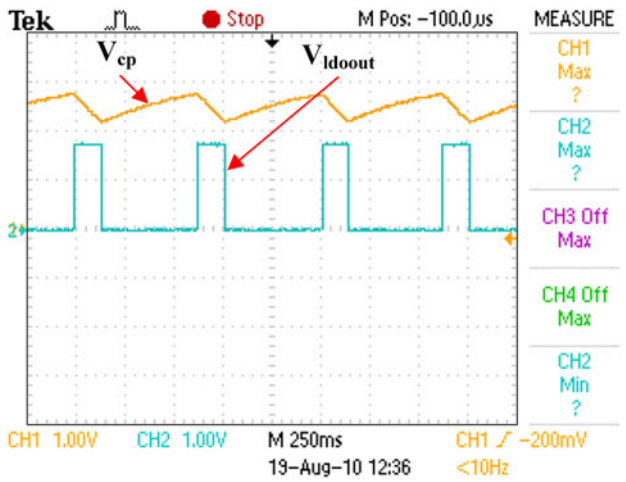

Fig. 15 Experimental responses of combining power management circuit and LDO circuit

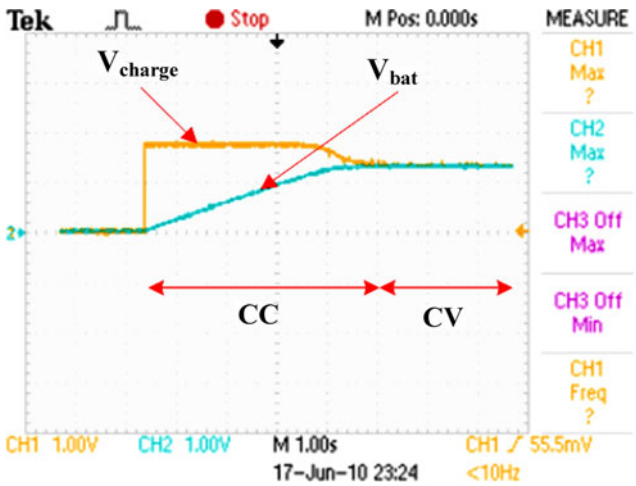

Fig. 16 Responses of the battery charger

voltage reaches a rated voltage which is close to 1.2 V, the charging process is switched to CV mode. The charger keeps the battery at a regulated voltage until the charging time is over. Thus, the battery can be charged to the designated voltage when the charging process is finished without the over-charging problem.

5 Conclusion and future works

A new energy harvest system that consists of a hula-hoop transformer, a micro-generator and an interface energy harvest circuit is designed and synthesized in this study. The transformer consists of mainly a main mass sprung in one translational direction and a free-moving mass attached at one end of a rod, the other end of which is hinged onto the main mass. It is capable of transforming linear reciprocating motions to rotary ones based on the concepts similar to the hula hoop motions. A miniaturized rotary generator in size of $10 \times 10 \times 2$ mm^3 and its compact energy harvest circuit chip is also successfully designed, fabricated and tested. The generator offers 4.5 V and 7.23 mW in rms at 10,000 rpm. The novel energy harvest circuit employing a new dual phase charge pump, power management circuit, a low dropout regulator and battery charger. This charge pump circuit owns the merit of automatic conversion of low-power AC signals by the micro-generator to DC ones. Experimental results show excellent performance of the synthesized system in terms of transforming reciprocating vibratory energy to DC power.

In the future, the presented circuit will be integrated with the hula-hoop mechanical device and the generator in the future in a single package. The current study shows the feasibility of the system. To be commercialized, the sizes of the hula-hoop and generator will be further optimized for given uses. As for the circuit, due to nature of 0.35 µm TSMC fabrication process, there are some limitation on the circuit proposed in this study. For instance, (1) it only accepts power with voltage under 3.3 V; (2) if there is loading, further battery management circuit has to been designed; (3) Power consumption has to be minimized. Alternative diodes with smaller cross voltages to save power are first be considered.

Acknowledgments The authors appreciate the support from National Science Council of R.O.C under the grant no. NSC 97-2221-E-007-050, and are grateful to the National Center of High-performance Computing for providing excellent computation capacity and National Chip Implementation Center (CIC) of Taiwan for implementing the energy harvest circuit. This work was supported in part by the UST-UCSD International Center of Excellence in Advanced Bioengineering sponsored by the Taiwan National Science Council I-RiCE Program under grant no: NSC-99-2911-I-010-101.

References

Arnold DP (2007) Review of microscale magnetic power generation. IEEE Trans Magn 43(11):3940–3951

Belendez A, Hernandez A, Belendez T, Neipp C, Marquez A (2007) Application of the homotopy perturbation method to the nonlinear pendulum. Eur J Phys 28:93–104

Dickson JF (1976) On-chip high-voltage generation in MNOS integrated circuits using an improved voltage multiplier technique. IEEE J Solid-State Circuits 11(3):374–378

Hatwal H, Mallik AK, Ghosh A (1983) Forced nonlinear oscillations of an autoparametric system—part 1: periodic responses. J Appl Mech 50:657–662

Jose SM, Mur-mir JO, Amirtharajah R, Ch AP, Lang JH (2001) Vibration-to-electric energy conversion. IEEE Trans Very Large Scale Integr (VLSI) Syst 9:64–76

Kulah H, Najafi K (2008) Energy scavenging from low-frequency vibrations by using frequency up-conversion for wireless sensor applications. J IEEE Sens 8(3):261–268

Leonov V, Torfs T, Fiorini P, Van Hoof C, IMEC L (2007) Thermoelectric converters of human warmth for self-powered wireless sensor nodes. IEEE Sens J 7(5):650–657

Lu CX, Wang CC, Chao Paul CP, Sung CK (2009) Dynamic analysis of a motion transformer mimicking a hula hoop. ASME IDETC & CIE, San Diego, CA, USA, pp 413–420

Liao LD, Chao Paul CP, Chen JT, Chen WD, Hsu WH, Chiu CW, Lin CT (2009) A miniaturized electromagnetic generator with planar coils and its energy harvest circuit. IEEE Trans Magn 45(10):4621–4627

Ottman GK, Hofmann HF, Lesieutre GA (2003) Optimized piezoelectric energy harvesting circuit using step-down converter in discontinuous conduction mode. IEEE Trans Power Electron 18(2):696–703

Peters C, Spreemann D, Ortmanns M (2008) A CMOS integrated voltage and power efficient AC/DC converter for energy harvesting applications. J Micromech Microeng 18:104005

Sasaki K, Osaki Y, Okazaki J, Hosoka H, Itao K (2005) Vibration-based automatic power-generation system. Micosyst Technol 11(8):965–969

Shameli A, Sasarian A, Rofougaran A, Rofougaran M, De Flaviis F (2007) Power harvester design for passive UHF RFID tag using a voltage boosting technique. IEEE Trans Microw Theory Tech 55(6):1089–1097

Shaw SW, Schmitz PM, Haddow AG (2006) Tautochronic vibration absorbers for rotating systems. J Comput Nonlinear Dyn 1:283–293

Shin J, Chung IY, Park YJ, Min HS (2000) A new charge pump without degradation in threshold voltage due to body effect. IEEE J Solid-State Circuits 35(8):1227

Spreemann D, Manoli Y, Folkmer B, Mintenbeck D (2006) Non-resonant vibration conversion. J Micromech Microeng 16:169–173

Sudou M, Takao H, Sawada K, Ishida M (2008) A novel RF induced power supply system for monolithically integrated ubiquitous micro sensor nodes. Sens Actuators A Phys 145:343–348

Yoshitake Y, Ishibashi T, Fukushima A (2004) Vibration control and electricity generating device using a number of hula-hoops and generators. J Sound Vib 275(1–2):77–78